Available on the CERN CDS information server **CMS PAS LUM-13-001**

CMS Physics Analysis Summary

Contact: cms-pog-conveners-lum@cern.ch 2013/09/07

CMS Luminosity Based on Pixel Cluster Counting - Summer 2013 Update

The CMS Collaboration

Abstract

The measurement of the LHC luminosity delivered to CMS in the 2012 proton-proton physics run is presented. Results are based on cluster counting from the silicon pixel detector. The luminosity calibration is updated using the Van der Meer scans performed in November 2012. The overall uncertainty on the integrated luminosity is estimated to be 2.5% (syst.) + 0.5% (stat.).

1 Introduction

The estimation of the luminosity delivered by the LHC relies on the precise measurement of the rate of specific "events":

$$L = \frac{R}{\sigma_0(E)A(t,\mu,n_b,..)} \tag{1}$$

We define the quantity that relates the measured rates to luminosity to be the visible cross section, $\sigma_{vis} = \sigma_0(E)A(t,\mu,n_b,..)$, where $A(t,\mu,n_b,..)$ is the acceptance as a function of time and event rate. The ideal luminometer should have no dependence of σ_{vis} on time and experimental conditions such as pileup (μ) or the filling scheme (n_b).

In CMS two detectors are exploited for the luminosity measurement: the forward hadronic calorimeter (HF), featuring a dedicated high rate acquisition system independent from the central DAQ and capable of estimating the luminosity per bunch, and the silicon pixel detector characterized by very low occupancy and excellent stability over time. Those two systems will be described in Section 2.

Thanks to its very small dependence on pileup and other experimental conditions, the counting of the pixel clusters is chosen for the precision offline luminosity measurement. The HF measurements benefit from smaller statistically uncertainty and can be useful for cross checks or systematic studies. This document describes in details the calibration of the cluster counting method by means of the Van der Meer (VdM) scan technique (Sections 3 and 4) and the integration of the instantaneous luminosity measurement over the 2012 LHC proton-proton run (Section 5). In Section 6, the systematic uncertainties related to both luminosity calibration and integration are discussed and evaluated.

Several aspects of this analysis represent a follow-up of previous studies. These studies are documented in [1] and references therein.

2 CMS luminometers

2.1 Forward Calorimeter

The (Hadron) Forward Calorimeter - HF - is part of the CMS Hadron Calorimeter, HCAL, and covers pseudorapidity $3 < |\eta| < 5$. Each HF endcap is divided into 36 segments in azimuth and 12 segments in η, each corresponding to a physical channel. Signals from the HF Photo Multiplier Tubes, PMTs, are digitized on a bunch-by-bunch basis using a QIE (charge integrator and encoder) chip, and then routed to a set of 36 HCAL Trigger and Readout (HTR) boards, each of which services 24 HF physical towers. In order to derive the luminosity signal from the HTR, an additional mezzanine board, called the HF luminosity transmitter (HLX), is mounted on each of the HTR boards.

The detector safely operates with unstable beams and thus can be used in on-line measurements. The real-time luminosity measurement based on HF can determine the average luminosity with a 1% statistical accuracy in less than 1s. The HF based luminosity, however, is subject to calibration drift as a result of gain changes in the HF PMTs and also other effects. Such drifts typically occur over a long period of time. In addition, the detector response has been proved to be non-linear with pileup in the luminosity regime of the 2012 LHC run. These two effects together make the usage of HF difficult to measure the luminosity with a high accuracy.

2.2 Silicon Pixel detector

The pixel detector contains approximately 66 million pixels (pixel cells) with dimensions $100 \times 150^{-}\text{m}^2$ each. It is the closest detector to the beam pipe, with cylindrical layers at 4cm, 7cm and 11cm and disks at either end extending to 2.5 in $|\eta|$. It can only operate at stable beam conditions. Thus it is only suitable for offline measurements. At design luminosity of $10^{34}\text{cm}^{-2}\text{s}^{-1}$, the detector occupancy is less than 0.1% on average (the average number of clusters per minimum bias interaction is about 200 and the average number of pixels per cluster is about 5).

The very low occupancy leads to an excellent linear detector response with increasing LHC luminosity. The detector is also extremely stable throughout the whole data taking.

2.2.1 Pixel Cluster Counting method

Luminosity is evaluated from the number of pixel clusters occurring on average in a zero-bias event (i.e. an event triggered by requiring only that two bunches cross at the CMS IP). The per-bunch instantaneous luminosity L is proportional to the number of collisions per crossing (μ):

$$\nu\mu = L\sigma_T \tag{2}$$

with $\nu = 11246\text{Hz}$ the beam revolution frequency and σ_T the total inelastic cross section. We define the average number of clusters per event as $\langle n \rangle = \mu n_1$ with n_1 the average number of clusters per inelastic collision and the visible cross section as $\sigma_{vis} = \sigma_T n_1$. The luminosity can then be estimated from the measurement of $\langle n \rangle$:

$$L = \frac{\nu \langle n \rangle}{\sigma_{vis}} \tag{3}$$

The visible cross section is calibrated by means of the VdM scan procedure and is the subject of the next section.

In order to guarantee a negligible time dependence of σ_{vis} the same detector configuration is used during data-taking as during the calibration scan. Only the pixel modules that functioned properly throughout the entire data taking period are considered for the luminosity measurement.

As in the previous analyses, the innermost barrel layer has been excluded in order to avoid problems with dynamic inefficiencies occurring at high instantaneous luminosity (Section 6.2). With respect to the analysis described in [1] the cluster definition was optimized to achieve a better stability against noise and dynamic inefficiencies.

3 Absolute Luminosity Calibration

The absolute luminosity calibration, i.e. the determination of σ_{vis}, requires the simultaneous measurement of the rates ($\langle n \rangle$ in the case of the cluster counting method) and the luminosity itself. The latter is given by a rather complicated formula involving several beam parameters, most importantly the charge density functions $\rho(\vec{r}, t)$:

$$L = \nu N_1 N_2 K(\vec{v}_1\, \vec{v}_2) \int \rho_1(\vec{r} - \Delta\vec{r}) \rho_2(\vec{r}, t) d^3\vec{r} dt \tag{4}$$

with ν the revolution frequency, $N_1 N_2$ the product of the protons population in the two beams[1], $K(\vec{v}_1\, \vec{v}_2)$ the kinetic factor dependent on the beam velocities and $\Delta\vec{r} \equiv (\Delta x, \Delta y, 0)$ the nominal

[1] In this note we typically refer to $N_1 N_2$ as "current" product (as this is actually what the beam instrumentation measures). This regardless the fact that the latter would be $N_1 N_2 \nu^2$.

separations between the two beams in the transverse plane. The integration in Eq. 4 can be carried out easily assuming Gaussian shapes for the charge densities:

$$L(\Delta x, \Delta y) = \frac{\nu N_1 N_2}{2\pi\Sigma_x\Sigma_y} \exp -\frac{\Delta x^2}{2\Sigma_x^2} \exp -\frac{\Delta y^2}{2\Sigma_y^2} \tag{5}$$

Eq. 5 is the basis of the VdM technique that ultimately consists in deriving the beam overlap (i.e. the product $\Sigma_x\Sigma_y$) from the shape of the measured rates as a function of the beam separation (rate profiles), obtained by scanning the beams one across the other along the horizontal and vertical planes. For most of the functional forms that can reasonably describe the beam shape it is possible to analytically define a relation between the width of the rate profile and $\Sigma_{x,y}$. During a VdM scan the transverse coordinates are scanned one at the time, a choice justified by the standard hypothesis on the possibility to factorize the density functions:

$$\rho(\vec{r}) = \rho(x)\rho(y)\rho(z) \tag{6}$$

The data can also be analyzed in the case that assumption cannot be made but the whole treatment becomes more complex and subtle systematics effects occur that inevitably compromise the accuracy of the measurement.

The pixel cluster counting visible cross section is derived combining Eqs. 3 and 7:

$$\sigma_{vis} = \frac{2\pi\Sigma_x\Sigma_y\langle n\rangle_{\Delta=0}}{N_1 N_2} \tag{7}$$

where $\langle n\rangle_{\Delta=0}$ is obtained from the amplitude of the rate profile and N_1N_2 is very accurately measured by the LHC beam current transformers (DCBCT and FBCT) [2] [3].

3.1 2012 Van der Meer scan campaigns

The accurate determination of σ_{vis} requires the performance of beam scans in dedicated conditions allowing the reduction of the sources of systematic effects from potentially spoiling the calibration procedure.

During each campaign, a better knowledge of the contributions degrading the corresponding measurement was determined and these effects were then addressed in subsequent campaigns. Just on the basis of these improvements, it is reasonable to expect the latest VdM scan to be better than the previous ones.

After detailed investigation it turned out that the scans in April and July do not allow the factorization of the beam shapes, Eq. 6. In the following sections we review the quality of the three VdM scan and the choice of relying exclusively on the data gathered in November is discussed and justified.

3.1.1 Critical overview of the 2012 scan campaigns

Several aspects are considered in the preparation of the beams and machine conditions for a VdM scan. The choice of filling scheme and number of protons per bunch reflects the needs of limiting the pileup at null separation, avoiding long range beam-beam effects and matching the optimal working point for the beam current transformers. Gaussian shaped beams are also highly preferable: only during the November VdM scan special efforts have been put to address that.

The evolution during the scan of the luminous region, defined as the 3D space distribution of the reconstructed primary vertices, can provide useful insight on the beams shapes. During a

simultaneous scan (i.e. when the beams are moved simultaneously), in the case of equal size single Gaussian beams, the centroid (beam-spot) and the width of the luminous region remains constant. As proved by Monte Carlo simulation, non trivial correlation among X and Y would induce luminous region distortion depending on the beam separation.

The plots of Figs. 1 and 2 compare respectively the beam-spot longitudinal coordinate and the luminous region vertical width as a function of the beam separation in the horizontal plane for the April (left) and the November (right) VdM scans. The left plot in Fig. 1 demonstrates the strong correlation introduced by the the crossing angle in the scan plane (at nominal value in April, null in November). The shift of the beam spot may lead to loss in acceptance. The sinusoidal shape of the data points in the left plot of Fig. 2 is a strong indication of invalidity of the assumption in Eq. 6. In contrast, the right plot suggests that the beam shapes in the November scan can be cleanly factorized.

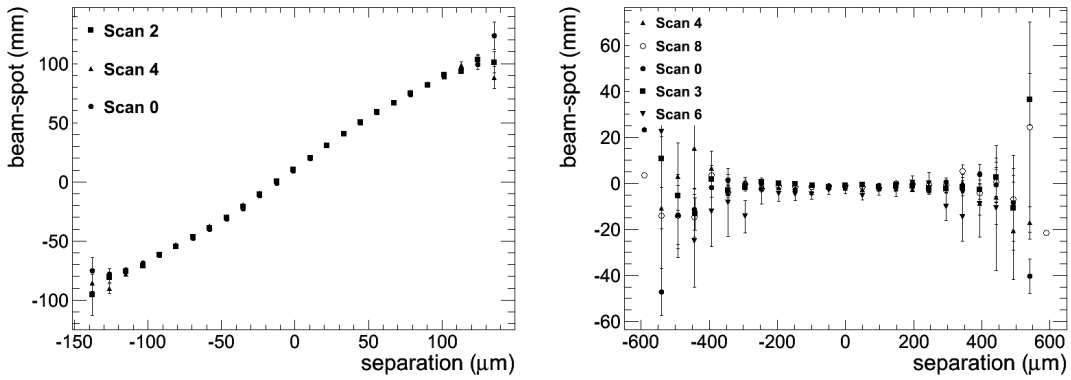

Figure 1: Beam-spot centroid longitudinal position as a function of the beam separation during a horizontal scan during the April (left) and the Nov. (right) campaigns. The strong correlation as observed in the April scan is due to the finite crossing angle.

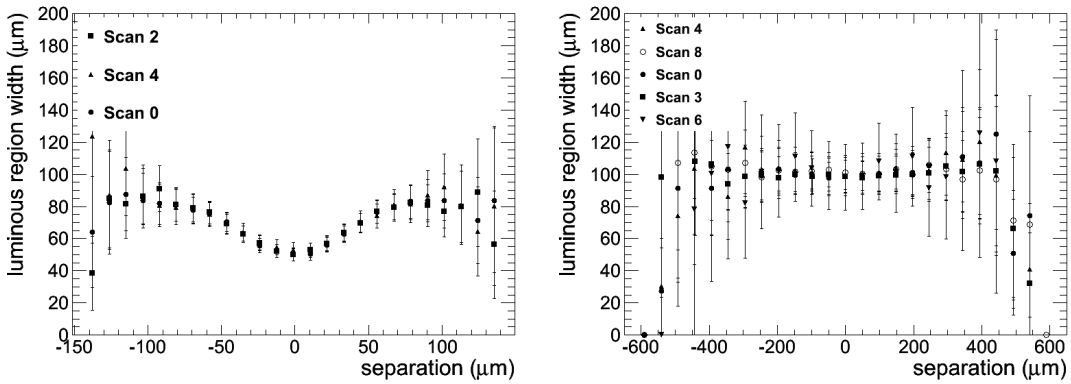

Figure 2: Luminous region RMS in the vertical plane as a function of the beam separation during a horizontal scan during the April (left) and the Nov. (right) campaigns. Non-factorisable beam charge density distributions are expected to produce correlations as observed in the April scan.

The main problem caused by non-factorisable beam shapes is the correct choice of the fitting function for the rate profiles. As shown in [1], the outcome of the fits varies substantially depending on the functional form of the fit function. In particular, in the case of the April scan, if Eq. 6 is nonetheless assumed to hold and 1D single or double Gaussian are used, a clear

trend is observed by the estimated visible cross section as a function of time (Fig.3 in [1]). Such behavior is now believed to be due to a sort of entropic dissipation of the X-Y correlations [4, 5].

Two dimensional fitting functions can be tried, whose parameters, however, can only be partially constrained by the data as the scan is only performed along the vertical and horizontal axes (an experimentally unfeasible mapping of the full transverse plane would be needed).

The excellent quality of the November scan was achieved thanks to several improvements in the beam and machine preparation with respect to April and July:

- reduce strength of the octuple magnets (less non-linear effects induced on the beams),
- LHC injection chain tuned to produce highly Gaussian bunches of moderate intensity ($8 - 9 \times 10^{10}\, p$/bunch) and modestly enlarged emittance ($\epsilon \sim 2.5 - 3\,\mu$m-rad) [6],
- no profile monitor screens in the transfer lines between the LHC injectors (avoiding to generate multiple-scattering-induced non-Gaussian tails).

In light of our discussion, we discard the April and July scan data as being affected by non-trivial systematics effects and rely entirely on the November scan to determine the absolute luminosity calibration.

3.1.2 November VdM scan

The VdM scan for CMS in November was performed during the LHC fill 3316 and consisted of five pairs of scans in the horizontal and vertical directions. Out of the five scans, three had nominally null separation in the plane orthogonal to the scan direction (head-on scans). During the third and the forth scan the beams were separated respectively by 148μm and 295μm in the orthogonal plane (offset scans). Each individual scan was performed by moving both beams at the same time one against the other (simultaneous scan), starting with beam 1 and beam 2 separated by $\Delta = 600\mu$m (6 nominal beam widths) and progressively reaching $\Delta = -600\mu$m in steps of half beam width. Each of the 25 scan points was maintained for 30 seconds.

The sketch in Fig. 3 represents the series of ten individual scans performed during fill 3316.

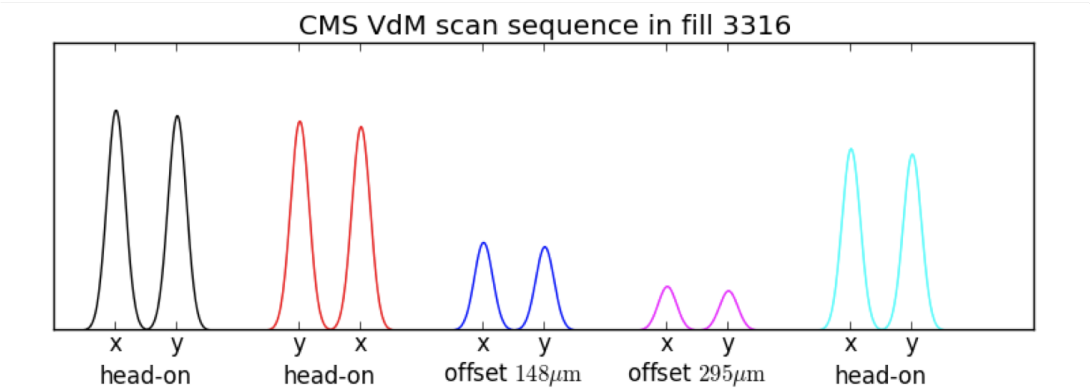

Figure 3: Overview of the November VdM scans. The horizontal axis of the sketch lists the conditions of the scan (the axis of the scan and the offset), while the size of the peaks indicates the relative size of the observed rate.

The beams were left at injections optics after the ramp to nominal energy (i.e. with $\beta^* = 11$m) and were taken into collision with no crossing angle. The filling scheme was such that 29

bunches were colliding in IP5 out of a total of 39.

CMS employed a dedicated trigger menu, recording data only for a subset of five bunch crossings (BX). The zero-bias trigger was configured in order to deliver 2kHz of accepted events.

3.2 Determination of σ_{vis}

Out of the five scan pairs performed in November 2012 only the three head-on scans are used to compute the beam overlap. The offset scans were intended to study possible non-linear effects and the derivation of an accurate luminosity calibration would require special treatment.

The profiles of the rate versus beam separation were fitted individually for each bunch crossing recorded by CMS and each scan pair. The peak instantaneous luminosity diminishes during a fill, due to protons loss (burn off and collimation cleaning) and to emittance growth. The quantities that via Eq. 7 lead to σ_{vis} need thus to be evaluated at a common time. The currents monitoring information is used to normalized each individual rate measurement, whereas as explained in Section 4.3, the two rate profiles of each scan pair are rescaled according to the estimated emittance evolution. The X and Y rate profiles are thus fitted simultaneously with a common amplitude parameter. Prior to the fit, a set of corrections are applied to the profile data. Such corrections are described in the next section.

A single Gaussian plus flat background is used as the fitting function. A detailed discussion of the systematic effects related to this choice will follow in Section 6.1. The plots in Fig. 4 show an example of the rate profile fit, whereas Table 1 summarizes the result of all the fits. For each bunch and each scan pair (15 measurements), the amplitudes (dimensionless, corresponding to $\langle n \rangle_{\Delta=0}/N_1N_2$ and reported in the table multiplied by 10^{22}) and the widths are used in Eq. 5 to provide an estimate for σ_{vis}.

Each recorded BX has its own features in terms of transverse emittances (i.e. sizes) and proton population both varying bunch to bunch up to a large factor (30% for LHC physics fills, typically less for a VdM scan fill). The former affects the rate profile widths, whereas the latter the amplitudes. The expected time trend, in which the beam widths increase and the peak luminosity decrease, are also evident.

Estimates for σ_{vis} can be derived from the beam overlaps and the amplitudes obtained from each BX and each scan pair. The plot in Fig. 5 displays the individual σ_{vis} with measurements, which are statistically compatible. Unlike the April scan, no clear trend is observed, confirming the hypothesis that possible non trivial correlations between the transverse coordinates are not relevant.

The value of the visible cross section is determined from the weighed average of the individual estimates to be 7.230 ± 0.038 barn. The error is statistical from the various measurements.

4 VdM scan Corrections

In this section, the corrections that need to be applied to the data collected during the November VdM scan are described. Both the rates and the nominal beam separation may require adjustments, which are implemented prior to the fit. Rigorously speaking, the order of application of the corrections would matter, but the size of the corrections is such that the ordering has no appreciable effect. The impact of each correction is evaluated by comparing the nominal value of σ_{vis} with the one obtained without that specific correction.

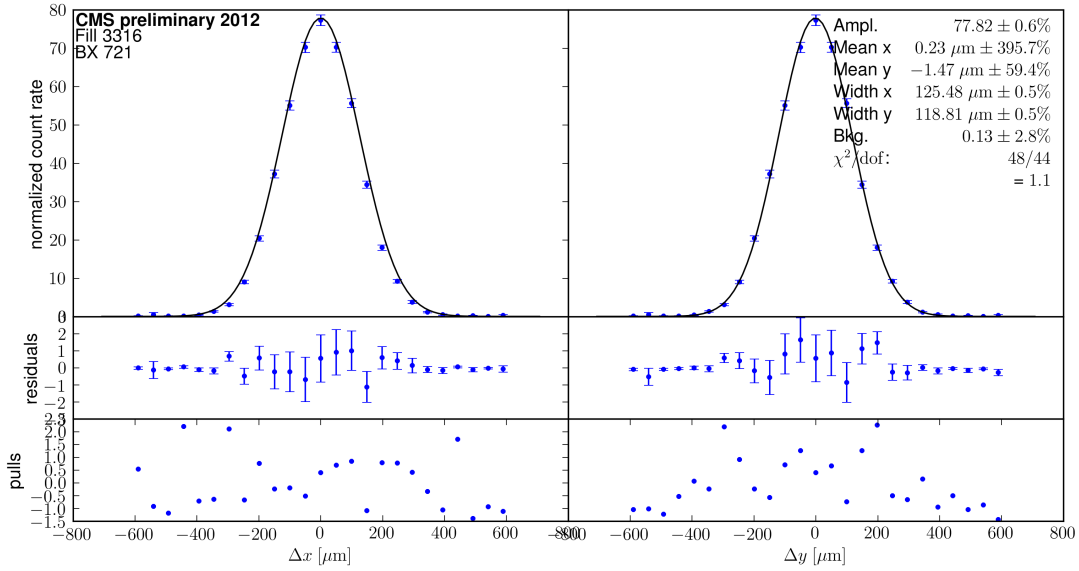

Figure 4: Example of a rate profile fit. This specific case corresponds to BX 721 and scan pair number 0.

Table 1: Fit results for the Van der Meer scan performed in fill 3316.

.

BX	Scan pair	χ^2/N_{dof}	Amplitude	Δ [%]	X mean [μm]	X width [μm]	Δ [%]	Y mean [μm]	Y width [μm]	Δ [%]
	0	1.4	76.2±0.5	-	-0.4 ± 1.0	126.34 ± 0.6	-	-0.6 ± 0.9	120.32 ± 0.6	-
	1	1.4	75.1±0.5	-1.4	1.9 ± 1.0	128.18 ± 0.6	1.5	-5.5 ± 1.0	120.16 ± 0.6	-0.1
1	4	0.8	72.2±0.5	-5.3	1.2 ± 1.1	128.61 ± 0.7	1.8	-1.0 ± 1.0	123.72 ± 0.7	2.8
	0	1.1	77.4±0.5	-	0.2 ± 0.9	125.35 ± 0.6	-	-1.5 ± 0.9	118.62 ± 0.6	-
	1	1.8	76.5±0.5	-1.2	0.8 ± 0.9	126.53 ± 0.6	0.9	-1.2 ± 0.9	118.77 ± 0.6	0.1
721	4	1.7	73.2±0.5	-5.4	2.0 ± 1.0	127.76 ± 0.6	1.9	1.6 ± 0.9	123.10 ± 0.7	3.8
	0	1.5	77.7±0.5	-	-0.7 ± 0.9	125.31 ± 0.6	-	0.7 ± 0.9	118.96 ± 0.6	-
	1	1.2	75.8±0.5	-2.4	-0.5 ± 0.9	126.07 ± 0.6	0.6	-4.2 ± 0.9	119.74 ± 0.6	0.7
1621	4	1.1	73.7±0.5	-5.2	-1.3 ± 0.9	127.50 ± 0.7	1.7	0.3 ± 0.9	123.00 ± 0.6	3.4
	0	1.7	77.4±0.5	-	0.6 ± 0.9	125.78 ± 0.6	-	0.1 ± 0.9	119.11 ± 0.6	-
	1	1.8	76.2±0.5	-1.6	-1.4 ± 0.9	125.75 ± 0.6	-0.0	-5.2 ± 0.9	119.47 ± 0.6	0.3
2161	4	0.9	73.5±0.5	-5.1	2.5 ± 0.9	128.15 ± 0.6	1.9	1.0 ± 0.9	121.43 ± 0.6	1.9
	0	1.1	80.1±0.5	-	-0.6 ± 0.9	121.90 ± 0.6	-	-1.2 ± 0.9	117.03 ± 0.6	-
	1	2.1	78.7±0.5	-1.7	0.2 ± 0.9	124.50 ± 0.6	2.1	-2.4 ± 0.9	117.30 ± 0.6	0.2
2881	4	0.9	74.9±0.5	-6.5	2.7 ± 1.0	125.64 ± 0.6	3.1	0.8 ± 0.9	121.51 ± 0.6	3.8

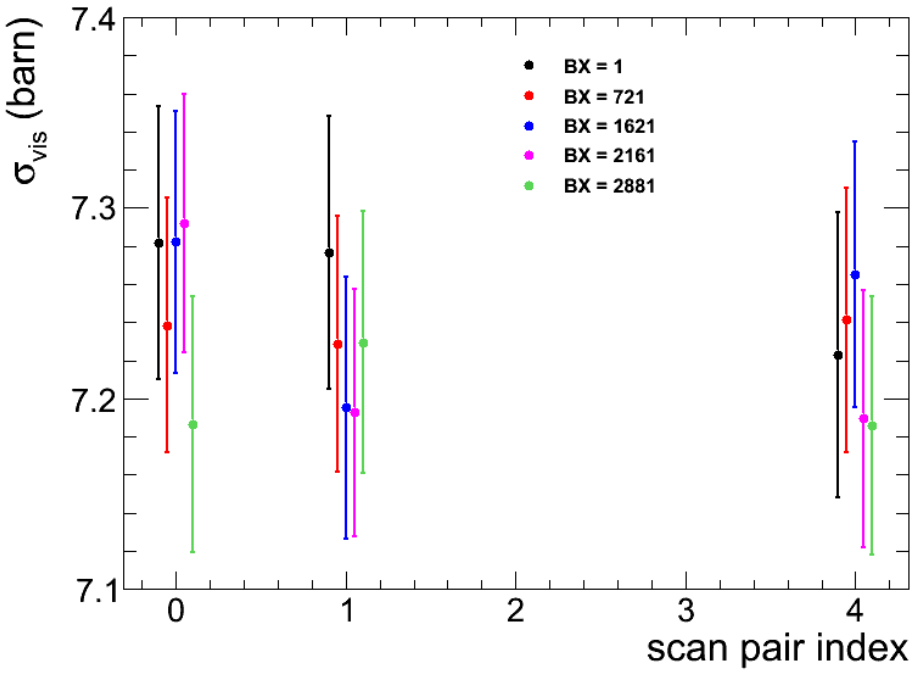

Figure 5: Estimates for σ_{vis} for each BX and head-on scan pair performed during fill 3316. The first four scans (two scan pairs) occurred consecutively within $\sim$ 1h, the last scan pair took place $\sim$ 2h later.

4.1 Length scale calibration

The nominal beam separation is derived from the LHC orbit knobs and is expected to be accurate to the level of a few percent. To achieve a better accuracy, the absolute scale can be calibrated using the measurements of the central tracking system as a reference. The same procedure adopted in the previous analyzes [1] [7] was repeated to compute the length scale corrections for the 2012 VdM scan campaigns. Two dedicated length calibration scans were performed during the LHC fills 2576 and 2855, the former at nominal optics ($\beta^* = 0.6$m) and the latter at $\beta^* = 11$m. This technique is described in detail in [8] and consists of moving the beams back and forth in the horizontal and vertical directions, keeping them constantly separated by roughly $\sqrt{2}\sigma_b$ where σ_b is the estimated beam width. Such distance maximizes the luminosity sensitivity to the beams separation. By monitoring the luminosity variation during the scan and confronting the nominal movements of the beams with the position of the beam spot, it is possible to determine the correction for the nominal position of each of the two beams.

The plots in Fig. 6 show the measured beam-spot position versus the nominal beams centroid position for the horizontal (left) and vertical (right) scans. To a good approximation only the average length-scale correction factor matters for the analysis of simultaneous scans (following the notation of Ref. [8], only $\bar{\alpha}$ is considered, whereas ϵ is neglected). This factor can be derived directly from the slopes of the linear functions fitting the scan data.

The different step size is due to different β^* values in the two fills allowing a wider scan range for fill 2855. The same difference in β^* lies behind the larger uncertainties on the measured beam position in fill 2855. The difference in abscissa between the results from the different fills originates from the different LHC machine optics and is of no consequence for the calibration.

Table 2 summarizes the results of the analysis of the two length-scale calibration fills. Even

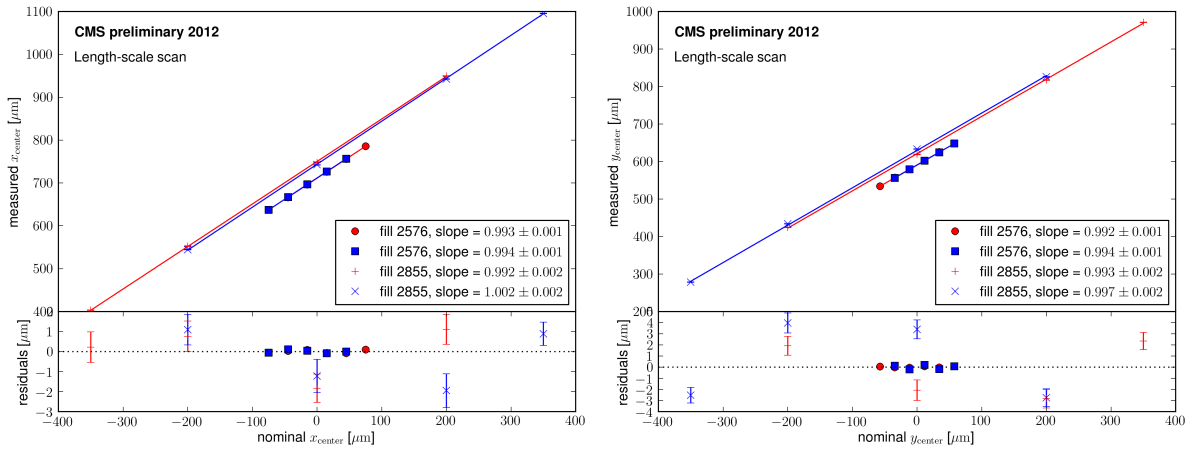

Figure 6: The relation between the measured center of the luminous region and the nominal crossing position for both scanning planes (left: horizontal, right: vertical) and both calibration fills. The two different markers/colors correspond to the two sets of scan points with opposite directions of approach.

Table 2: Length-scale calibration factors obtained from the scans are shown in Fig. 6. The quoted uncertainties correspond to the fit-parameter uncertainties.

Fill	Scan direction	X-plane	Y-plane
2576	low-to-high	0.993 ± 0.001	0.994 ± 0.001
	high-to-low	0.994 ± 0.001	0.992 ± 0.001
2855	low-to-high	1.002 ± 0.002	0.993 ± 0.002
	high-to-low	0.992 ± 0.002	0.997 ± 0.002

though the two data-sets provide consistent correction factors, for consistency only the fill with the same optics as the reference VdM scan are used. From fill 2855 we obtain the following correction factors: 0.997 ± 0.005 for the X-plane and 0.995 ± 0.002 for the Y-plane.

4.2 Ghosts and Satellites

The LHC beam currents are measured by dedicated devices. The DC beam-current transformer is capable of estimating the total current of each of the two beams with high accuracy (0.3%) [2], whereas the FBCT can measure the current of the individual bunches circulating in the machine [3]. The bunch population can vary up to 30% from one bunch to another, the current product used for the determination of the visible cross section needs then to be based on the FBCT data. The latter is, however, normalized such that the sum of the individual bunches matches what measured by the DC BCT.

Spurious charge can be present in the machine, either belonging to non colliding bunches (ghosts) or leaking out from the main RF bucket into a near-by bucket[2] (satellites). In both cases those protons are accounted for by the current transformers but do not contribute to a measurable luminosity.

The FBCT measurement of the bunch population is then corrected according to the following

[2] The LHC RF frequency is approximately 400 MHz, the 25 ns bunch slots are then actually composed by ten 2.5 ns long buckets.

formula:

$$N^j(t) = N^j_{FBCT} \frac{N_{DC}(1 - f_{ghost})}{\sum_j N^j_{FBCT}} (1 - f^j_{sat.}) \tag{8}$$

with f_{ghost} and $f^j_{sat.}$ respectively the fraction of ghost charge out of the total beam current and the fraction of satellite charge in bunch j. The spurious charge is measured by the LHC Longitudinal Density Monitor (LDM) [9]. The LDM data for fill 3316 indicates that both the ghost and the satellite charge was very limited [10]. The former is estimated to be $< 0.1\%$ for each of two beams and is neglected in Eq. 8. Results concerning $f^j_{sat.}$ for the bunch crossings relevant for this analysis are summarized in Table 3.

Table 3: Fraction of charge measured by the FBCT belonging to satellite buckets with respect the total bunch population as estimated from LDM [10]

BX	beam 1	beam 2
1	0.07%	0.40%
721	0.07%	0.37%
1621	0.08%	0.38%
2161	0.06%	0.35%
2881	0.09%	0.37%

A common factor $f_{sat.} = 0.4$ is applied to the bunches of beam 2, whereas no correction is applied for beam 1.

4.3 Emittance growth

The increase of beam emittance affects both the luminosity and the beam size, and thus respectively the rate profile amplitude and width. Beam profiles information coming from standard beam instrumentation is not complete for fill 3316, therefore the emittance variation is derived indirectly from other quantities.

The correction for the amplitude variation is computed assuming that the time dependency of the luminosity is carried by two components, the current product, N^2, and the emittance[3]. In all cases such dependency is assumed to be linear:

$$L(t) = L_0(1 + m_L t) = k\frac{N^2(t)}{\epsilon(t)} = k\frac{N_0^2(1 + m_{N^2} t)}{\epsilon_0(1 + m_\epsilon t)} \tag{9}$$

and hence

$$\frac{d\log L}{dt} = \frac{d\log N^2}{dt} - \frac{d\log \epsilon}{dt} \tag{10}$$

allowing determining the rate of variation of the emittance from those of the luminosity and beam current products:

$$m_{N^2} - m_L = m_\epsilon \tag{11}$$

The left plot in Fig. 7 shows the time dependency of the luminosity (as measured from the HF online system) and the current product (DC BCT measurement) during the first two scan pairs of fill 3316. Data are reported only for periods with the beams colliding head-on.

[3]What really matters for the amplitude of the rate profiles is the peak instantaneous luminosity. Given that each rate measurement is already normalized by the current product, we just need to estimate the additional factor contributing to the luminosity time dependency. Although a faithful assumption, the correspondence of that factor to the beam emittance is technically not necessary.

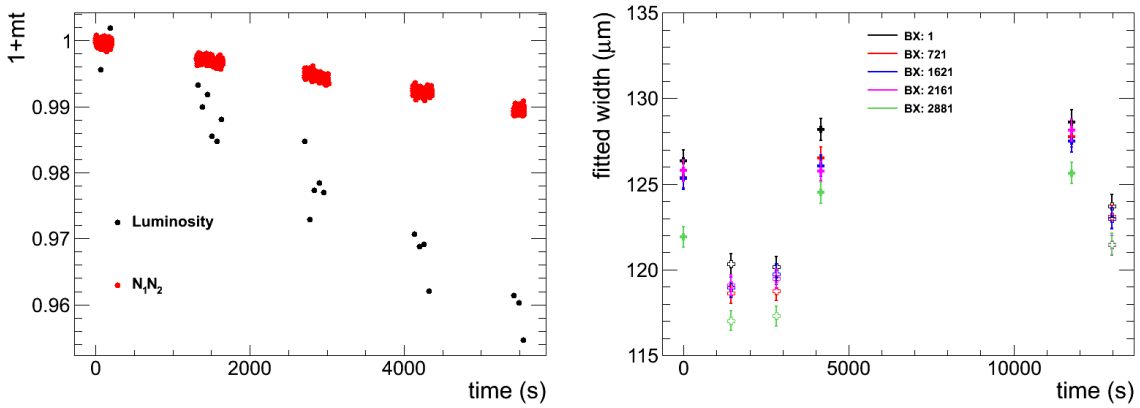

Figure 7: Left: time dependency of the luminosity (black) and the beam currents product (red). Right: time evolution of the rate profile widths for each BX considered in the analysis. Solid (empty) crosses stands for horizontal (vertical) scans.

The slopes obtained from a linear fit of the data result to be $m_L \sim -7 \cdot 10^{-6} s^{-1}$ and $m_{N^2} \sim -2 \cdot 10^{-6} s^{-1}$. From Eq. 11 we obtain $m_\epsilon \sim 5 \cdot 10^{-6} s^{-1}$. This coefficient is used to equalize the amplitudes of the first and the second scan in each scan pair. The rates of the two scans are scaled by a factor $1 \pm m_\epsilon \Delta t/2$ ($-$ for the first and $+$ for the second respectively), where Δt is the time elapsed between the two scans and is typically $\sim$ 1500 seconds. The correction improves the quality of the fit to the rate profiles, whereas the net effect on the luminosity calibration is numerically very small, $\sim 0.1\%$.

The amplitudes are then estimated in between the two horizontal and vertical scans for each scan pair; let's call this time t_0. This allows a simplified treatment of the effect of the emittance growth on the beam overlap. The quantities in Eq. 7 need to be considered at the same time, $t = t_0$ in our case. The widths however are estimated in different times, $\sim \Delta t$ apart from one another:

$$\Sigma_x(t_0)\Sigma_y(t_0) \rightarrow \Sigma_x(t_0 - \frac{\Delta t}{2})\Sigma_y(t_0 + \frac{\Delta t}{2}) \tag{12}$$

In accordance to what is supposed for the emittance, we assume for the beam overlaps $\Sigma_{x,y}(t)$ a linear dependence on time:

$$\Sigma_{x,y}(t) = \Sigma_{0;x,y}(1 + m_{\Sigma_{x,y}} t) \tag{13}$$

Estimating in Eq. 7 $\Sigma_{x,y}$ at times $t = t_0 \pm \Delta t/2$ implies a bias on σ_{vis} proportional to the difference between the vertical and horizontal emittance increase rates:

$$\frac{\delta(\sigma_{vis})}{\sigma_{vis}} \cong (m_{\Sigma_y} - m_{\Sigma_x})\frac{\Delta t}{2} \tag{14}$$

The coefficients $m_{\Sigma_{x,y}}$ are derived from the time evolution of the rate profile widths. Those are shown independently for each BX in the right plot of Fig. 7. The slopes obtained from each BX is averaged yielding $m_{\Sigma_x} = 2 \cdot 10^{-6} \mathrm{s}^{-1}$ and $m_{\Sigma_y} = 2.5 \cdot 10^{-6} \mathrm{s}^{-1}$ for the horizontal and vertical planes respectively. It is worth noticing that as expected $m_{\Sigma_x} + m_{\Sigma_y} \sim m_\epsilon$. From Eq. 14 the bias results small enough ($< 0.1\%$) to be neglected.

4.4 Orbit drift

The beam orbit is typically very stable during a fill, nonetheless even a small variation of the orbit during the scan can affect the beam overlap measurement. The orbit is constantly measured by Beam Position Monitors (BPM) along the LHC arcs. The BPM data can be used to extrapolate the beam positions at the interaction point (IP) to verify their stability. The procedure

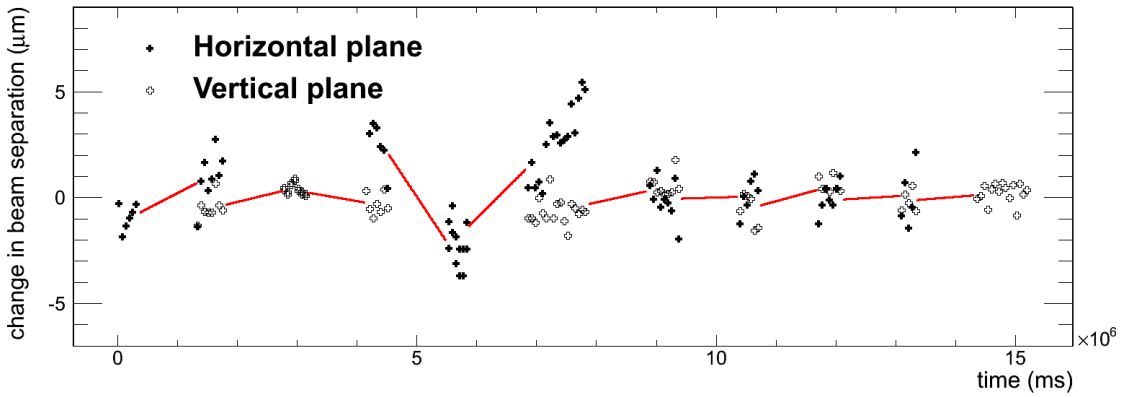

Figure 8: Difference of the estimated beams orbits at the CMS IP in the horizontal (solid crosses) and vertical (empty crosses).

described in [5, 11] has been followed. The plot in Fig. 8 shows the difference of the estimated orbits of the two beams at the CMS IP in the periods between the scans when the beams were colliding head on (the extrapolation of the orbits during a scan may not be reliable due the non perfect closure of the local bump). Data are displayed either for the vertical (empty crosses) or the horizontal plane (solid crosses) accordingly to direction of the in between scan.

The effect on the separation due to possible orbits drift during the scan is estimated by linearly interpolating the measurements before and after. The variation is small and the overall effect on σ_{vis} is $\sim$ 0.2%. The drifts of the beams along the plane orthogonal to the scan direction (affecting only the amplitude, irrelevant for the beam overlap estimation) are comparable in size with those estimated from Fig. 8 and therefore irrelevant for the determination of σ_{vis}.

4.5 Beam-beam effects

The formula in Eq. 4 does not take into account the electromagnetic forces between the beams when they cross each other. The so called "beam-beam" effects are expected to be smaller than during standard physics operations (due to reduced beam and bunch current), but the potential distortions of the rate profiles have to be evaluated.

The most sizable effect (beam-beam deflection) is the kick that each beam induces to the other when they are are separated in the transverse plane. The actual correction on the nominal separation is computed by means of an analytic formula estimated in close orbit conditions [4, 11]. The plot in Fig. 9 shows the beam-beam induced deflection in the scan plane as a function of the beam separation.

The abscissa of the rate profiles are corrected shifting the data points accordingly to the predictions of the analytic formula. The overall effect on σ_{vis} is around 1.5%.

In addition to dipole kick, the two beams also act on each other as (de)focusing quadrupoles (dynamic-β effect), affecting the β function and hence the luminosity. The correction for the measured rates are studied in [4, 5, 12][4]. Those calculations indicate that the effect on the visible cross section is expected to be very small, $\sim$ 0.2%. In view of the small size of the estimated effect and the uncertainties surrounding it, we have elected not to apply a correction, but rather have taken it into account by assigning an appropriate systematic error.

[4]Those references are being updated to include a (sizable) procedural correction.

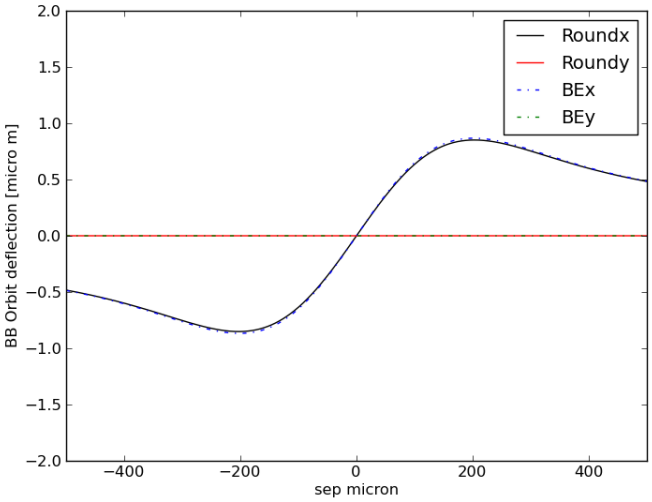

Figure 9: Left: Analytic estimation of the beam beam deflection as a function of the beam separation. for parameters typical of fill 3316.

5 Luminosity integration

A convenient minimal time interval to consider for the estimation of luminosity is the "luminosity section" (LS), defined as 2^{18} LHC orbits and corresponding $t_{LS} = 23.31$ seconds. For every LS the average number of clusters per event ($\langle n \rangle$) is computed and the luminosity for the LS is derived multiplied by t_{LS} what resulting from Eq.3.

The overall integrated luminosity for the 2012 physics run is then computed summing the luminosity of each LS recorded by CMS and considered good for offline physics measurements.

As discussed in Section 6.2, the stability of the pixel clusters counting method is expected to be very good. The only dependence of σ_{vis} on the LHC filling scheme that is worth addressing is due to a small out-of-time response of the pixel clusters. This 'afterglow' is discussed in the following section.

5.1 Afterglow correction

The pixel cluster counting method includes a small out-of-time response (or 'afterglow') that mainly arises from mild activation of the detector and the surrounding material. The modeling of the afterglow and the evaluation of its effect on the cluster counting method has been described in detail in [1]. That analysis has been repeated for the slightly different pixel cluster definition adopted here and the correction factors for the relevant filling schemes have been recomputed. The results are reported in Table 4 and are very similar to what obtained in [1].

For most physics running, where filling schemes with 1380 bunches are used, the typical correction is 2.3% with an uncertainty of 0.5%.

6 Systematic Uncertainties

In the following the systematic uncertainties related to luminosity absolute calibration and integration will be discussed and evaluated.

Table 4: Pixel afterglow correction factors for all LHC filling schemes used during 2012.

Filling Scheme	Correction Factor
Multi_48b_35_3_6_4bpi14inj	$0.999 \pm 0.0\%$
Multi_52b_3_24_24_4bpi13inj	$1.000 \pm 0.0\%$
50ns_72_60_0_6_36bpi4inj	$0.992 \pm 0.1\%$
50ns_78b_72_0_48_36bpi3inj	$0.991 \pm 0.1\%$
50ns_84b_72_0_60_36bpi3inj	$0.991 \pm 0.1\%$
50ns_88b_75_0_60_36bpi4inj	$0.991 \pm 0.1\%$
50ns_264b_249_0_240_36bpi8inj	$0.990 \pm 0.2\%$
50ns_480b_471_0_461_72bpi12inj	$0.984 \pm 0.3\%$
50ns_624b_618_0_604_72bpi12inj	$0.983 \pm 0.3\%$
50ns_840b_801_0_804_108bpi13inj	$0.983 \pm 0.3\%$
50ns_840b_807_0_816_108bpi12inj	$0.983 \pm 0.3\%$
50ns_852b_807_0_816_108bpi13inj	$0.983 \pm 0.3\%$
50ns_1092b_1051_0_1032_108bpi12inj	$0.980 \pm 0.4\%$
50ns_1092b_1054_0_1032_108bpi12inj	$0.980 \pm 0.4\%$
50ns_1374_1368_0_1262_144bpi12inj	$0.977 \pm 0.5\%$
50ns_1374_1368_0_1262_144bpi12inj_V2	$0.977 \pm 0.5\%$
50ns_1380b_1331_0_1320_144bpi12inj	$0.977 \pm 0.5\%$
50ns_1380b_1377_0_1274_144bpi12inj	$0.977 \pm 0.5\%$
50ns_1380b_1380_0_1274_144bpi12inj	$0.977 \pm 0.5\%$

6.1 Uncertainties related to σ_{vis}

The experience gathered in the three years of LHC running and from the many VdM scan campaigns performed since then demonstrated that the absolute calibration is by far the most delicate aspect of the luminosity measurement. Several subtle sources of systematic effects have been unveiled and one can not rule out the possibility that others will be uncovered. In the process of estimating the uncertainties it is surely wise to be cautious. As discussed in Section 3.1.1 the main reason that led to the choice of the November scan as the reference for the luminosity calibration stems from the non trivial correlation among the transverse coordinates of the bunches charge density functions. As verified a posteriori, such correlation had the tendency of fading out with time, introducing an apparent time dependence of the visible cross section. At the time, to cover this unexplained effect, an uncertainty of 4% was assigned in keeping with the variation of σ_{vis} among scan pairs.

6.1.1 Fit Model

The large uncertainties linked to the scan-to-scan variation in the April VdM campaign was ultimately caused by the inappropriate assumption on the function describing the bunch shapes. We know from several sources that the bunch shapes in fill 3316 were much more compatible with a single Gaussian function. This in particular limits the possibility of developing strong X-Y correlations. In particular, no trend is present in the visible cross section estimates (Fig. 5).

In order to check the dependence of σ_{vis} on the assumed fit function, we repeat the fit of the rate profiles as measured by the HF with a set of functions: single Gaussian plus constant ("SG"), double Gaussian plus constant ("DG") "supergaussian". The latter is defined as a series of pseudo Gaussian, $\exp -0.5(x/\sigma)^n$, with $n = 2, 4, ..$; in this study we considered the terms only

up to $n = 4$. Although all the indications support the assumption of Eq. 6, and therefore justifies the usage of one dimensional functions, it is well worth testing the results of a fit of a 2D function. In addition to these three 1D functions mentioned previously a 2D double Gaussian is also used to fit the rate profiles.

In all cases the fit quality is comparable (in terms of $\chi^2/NDoF$). The HF based rate profiles have been chosen to evaluate this check as they benefit from a lower statistical uncertainty. The consistency of the HF and pixel cluster counting fit results will be discussed in the next paragraph.

Table 5 summarizes the variation on the value of σ_{vis} for the three scan pairs obtained from the various fitting functions. The single Gaussian plus constant fit performed on scan pair 4 is using as reference. The dependency is indeed rather small, with σ_{vis} varying at most by 1.3% from the reference. Still the number of trial fitting functions is limited. Although of excellent quality, the November scan is the first of its kind. We have therefore conservatively assigned a 2% uncertainty in connection with the choice of fit model.

Table 5: Percent variation of σ_{vis} for the three scan pairs and for three fitting functions. The single Gaussian plus constant fit of scan pair 4 is used as reference.

	SG	DG	supergaussian	2D DG
scan pair 0	0.4%	0.4%	1.2%	0.2%
scan pair 1	-0.6%	-0.6%	0.6%	-0.4%
scan pair 4	-	0%	1.3%	0.1%

6.1.2 HF versus Cluster Counting comparison

The peak number of pileup events during the scan was intentionally very small, ~ 0.6, compared to the physics data taking configuration. In this regime the HF based luminosity measurement has a very linear response versus pileup. Therefore the rate profiles obtained from the cluster counting method and HF are in principle comparable. In order to assess an additional bias, we confront the widths of the scan profiles as measured from the two detectors. The comparison has been done for the three head-on scans pairs on the five bunch crossings available to the cluster counting, individually for the horizontal and vertical scans (a total of 30 measurements). The plot in Fig. 10 shows the distribution of the difference between of the widths as measured by the cluster counting method and by the HF divided by the statistical uncertainty. The latter is fully dominated by the cluster counting and corresponds to $\sim 0.5\%$ of the width. The RMS of the distribution is close to 1 and the mean value compatible with zero, demonstrating the excellent compatibility of the two methods.

6.1.3 VdM corrections

In Section 4 the various corrections applied to determine the visible cross sections out of the rate profiles were described. Each of those carries an uncertainty that only in a few cases can be estimated in a well defined and sound procedure. For the others we conservatively assume an error equal to half of the corresponding correction.

- **Beam currents:** the DCCT scale is known to a precision of 0.3% [2], the uncertainty on $f_{sat.}$ is then assumed to 50% of its value.
- **Length scale:** the uncertainty is derived from the statistical combination of the various measurements of the correction factor and correspond to 0.5%.

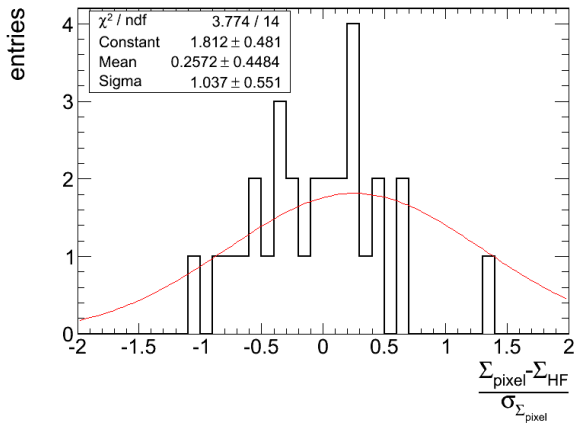

Figure 10: Distribution of the difference between of the rate profile widths as measured by the cluster counting method and by the HF divided by the statistical uncertainty.

- **Emittance growth:** the evaluation of Eq. 7 at a time in between the two scans of a scan pair is robust against emittance variations. We conservatively assume 0.2% as sytematics error.
- **Orbit drift:** the corresponding correction is very small, 50% of it is taken as uncertainty.
- **Beam-beam deflection:** a precise procedure has been developed in [4, 11] to assess the corresponding systematic uncertainty, which is estimated to be $\sim$ 30% of the correction.

As explained in Section 4.5 the corrections for the dynamic-β effects are not applied. The studies addressing that [4, 5, 12] are non trivial and although the bias is expected to be small we conservatively assume an uncertainty of 0.5%.

For scans where the beams were not perfectly overlapping in the plane orthogonal to the scan direction, but instead separated by an amount $\delta_\perp$, an additional factor $\exp(-\frac{\delta_\perp^2}{2\Sigma_\perp^2})$ should be considered. The fitted mean values reported in Table 1. are good estimates of the size of $\delta_\perp$. They do not exceed a few micron, i.e. a few percent of the beam overlap. The corresponding bias small enough to be neglected.

6.2 Uncertainties related to integration

As previously discussed, the reason for which the pixel detector is exploited as offline luminometer is its stability with time and against experimental conditions. In the following the accuracy with which we estimate the constancy of σ_{vis} is addressed.

6.2.1 Time Stability

As in the case of the previous analysis [1], the figure of merit to assess the stability of the pixel detector with time is the relative contribution of the four detector regions to the total cluster count. That is shown in the plot of Fig. 11 for all the physics runs in 2012. Each contribution is stable throughout the year to better than 1%.

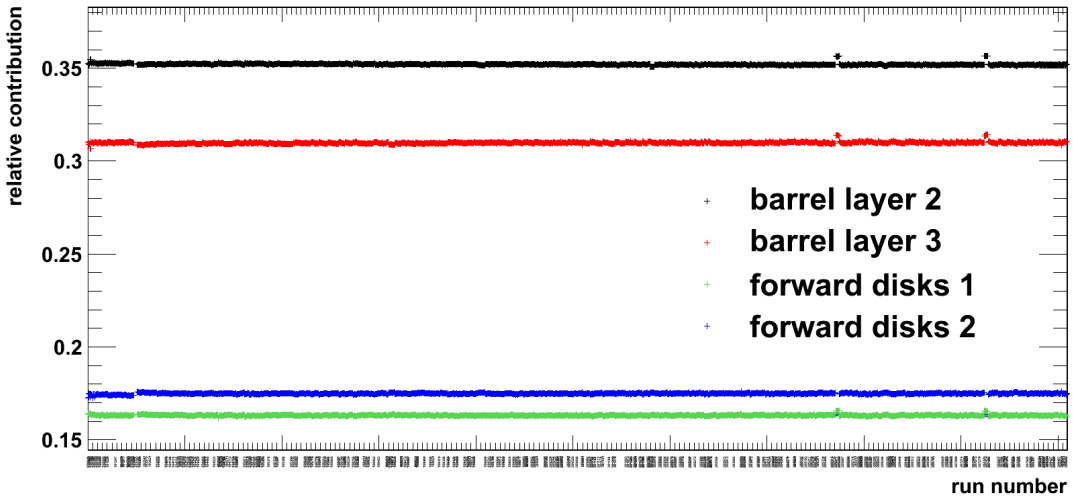

Figure 11: Relative contributions of different pixel detector regions to the total cluster count as a function of the run number for the 2012 physics runs.

6.2.2 Stability versus pileup

Although implicitly asserted in the previous paragraph, it is worth checking explicitly the potential dependency of the pixel cluster counting versus pileup. This is done by looking at the ratio of the relative contribution of the four pixel detector regions during a specific LHC fill (3236) where the luminosity varied significantly over the time. The plots in Fig. 12 show indeed the pileup (upper plot) and the variations of the relative contributions (lower plot) as a function of time. As it can be seen, fluctuations do not exceed the few per mill.

6.2.3 Dynamic inefficiency

Very high charged tracks multiplicity or very high L1 trigger rate can fill the read-out buffers of the pixel detectors which effectively result inefficient for short periods of time. These dynamic inefficiencies have been studied in detail in the past and their effect has been proved to be small. The plots in Fig. 13, show the drop of the pixel cluster efficiency as a function of the instantaneous luminosity (left) and trigger rate (right). The efficiency reduction for the first barrel layer is sizable and that is why the corresponding channels have not been included for the cluster counting. The other detector regions instead are much more stable, losing at most $\sim 0.5\%$.

6.2.4 Geometrical acceptance

The centroid of the luminous region can drift along the longitudinal direction either due to orbit effects (for instance jitter of the RF settings) or non head-on collisions in the horizontal plane with a finite crossing angle[5]. The jitter of the beam-spot along the longitudinal axis during the 2012 physics run was small as shown by the left plot of Fig. 14: the RMS of the distribution is 0.5 cm with a maximal excursion of $\sim$ 2 cm. Given the limited dimensions of the pixel detector, a dependence of its geometrical acceptance on the longitudinal position of the interaction vertex can be expected. Such dependence can be quantified on the basis of the

[5]That was the case for instance during the special run CMS set up to record lower luminosity data for the W and Z cross section measurement [13].

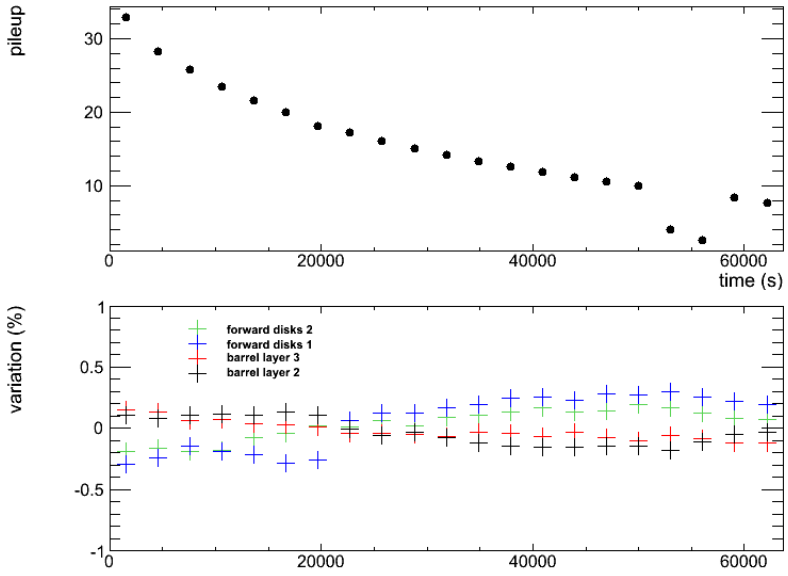

Figure 12: Pileup (upper plot) and relative contributions of different pixel detector regions (down) as a function of time during fill 3236. The drop in luminosity around 10h after the beginning is due to an end-of-fill VdM scan.

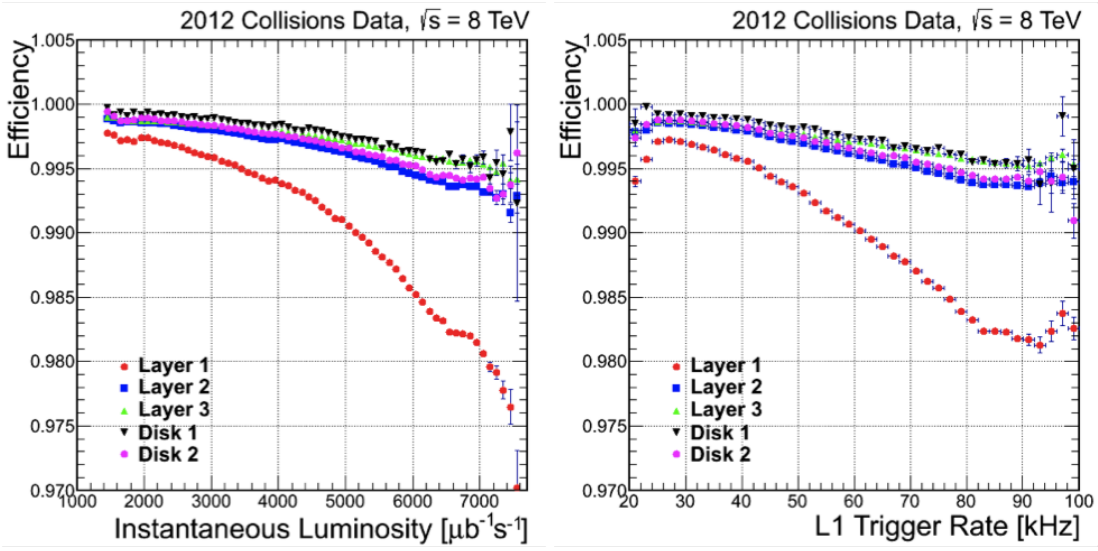

Figure 13: Pixel cluster efficiency drop for various detector components as a function of the instantaneous luminosity (left) and L1 trigger rate (right).

right plot in Fig. 14, where the average number of pixel clusters per collision is computed from a Monte Carlo sample of minimum bias events as a function of the generated interaction vertex position.

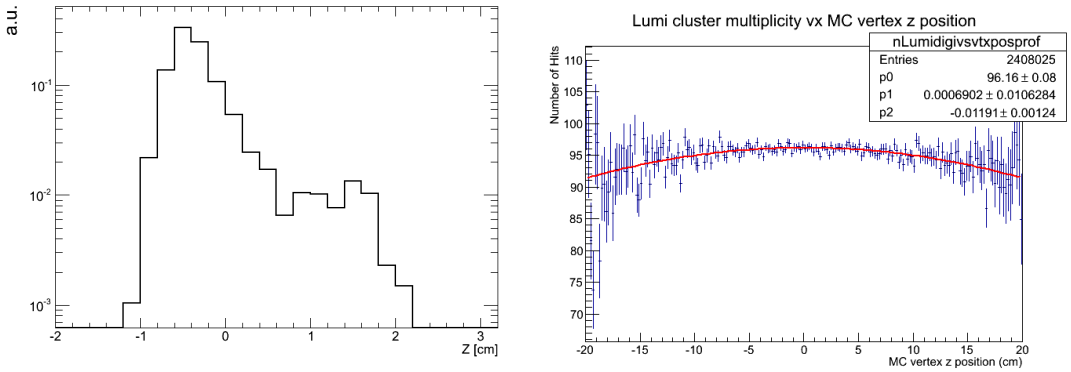

Figure 14: Left: distribution of the beam-spot in the longitudinal direction for the 2012 LHC run. Right: expected number of hits as a function of the longitudinal position of the generated interaction vertex.

The acceptance dependency on the longitudinal coordinate z is obtained from the parabolic function fitting the data of the right plot in Fig. 14:

$$A(z) = 1 + \frac{a}{c} z^2 \tag{15}$$

with $a = -0.012$, $c = 96$ cm^2. The effect of the geometric acceptance on the cluster counting from collisions produced by beams with a longitudinal shape $g(z)$ (a Gaussian with a width $\sigma_z = 5$ cm) colliding at a point $z = 0$ can be computed from the integral:

$$\int g(z)A(z)dz = 1 - \frac{a}{c}\int z^2 g(z)dz \sim 1 - \frac{\sigma_z^2 a}{c} \tag{16}$$

This factor is in good approximation the same for a typical physics run and the Nov VdM scan, therefore it must not be accounted for. The effect of the beam-spot jitter can be assessed by estimating the variation of the acceptance factor and integrating it over the excursion observed in 2012:

$$\int j(\delta)\int [g(z)A(z) - g(z-\delta)A(z)]dzd\delta = \int j(\delta)\int g(z)[A(z) - A(z+\delta)]dzd\delta = \int j(\delta)\frac{a\delta^2}{c}d\delta \tag{17}$$

where $j(\delta)$ is the density function describing the beam-spot jitter, left plot of Fig. 14. Conservatively we assume $j(\delta)$ to be a box function within the beam-spot excursion range, $\delta_{max}(\delta_{min}) = 2(-1)$ cm:

$$j(\delta) = \begin{cases} (\delta_{max} - \delta_{min})^{-1}, & \text{if } \delta_{min} < \delta < \delta_{max} \\ 0, & \text{otherwise} \end{cases} \tag{18}$$

The integration in Eq. 17 can then be easily carried out:

$$\int_{\delta_{min}}^{\delta_{max}} \frac{a\delta^2}{c(\delta_{max} - \delta_{min})}d\delta = \frac{a(\delta_{max}^3 - \delta_{min}^3)}{3c(\delta_{max} - \delta_{min})} \tag{19}$$

resulting in a negligible ($< 0.1\%$) effect of the overall geometrical acceptance on the cluster counting based luminosity estimate.

6.3 Systematic uncertainties overview

The individual systematic uncertainties related to σ_{vis} and to luminosity integration are summarized in Table 6. The total uncertainty is computed assuming those error to be uncorrelated and normally distributed, i.e. by the sum in quadrature of the individual contributions.

Table 6: Summary of the systematic errors. When applicable, the percentage correction (on σ_{vis} for normalization effects and on the total luminosity for the afterglow effect) is also reported.

	Systematic	correction (%)	uncertainty (%)
Integration	Stability	-	1
	Dynamic inefficiencies	-	0.5
	Afterglow	~ 2	0.5
Normalization	Fit model	-	2
	Beam current calibration	-	0.3
	Ghosts and satellites	-0.4	0.2
	Length scale	-0.9	0.5
	Emittance growth	-0.1	0.2
	Orbit Drift	0.2	0.1
	Beam-beam	1.5	0.5
	Dynamic-β	-	0.5
	Total		2.5

7 Summary

The analysis of the pixel data have been presented aiming at estimating the luminosity gathered by CMS during the 2012 proton-proton LHC run. The measurement relied on the pixel cluster counting method whose absolute calibration has been determined by means of the Van der Meer scan performed in November 2012 during the LHC fill 3316. The uncertainties related to both calibration and luminosity integration have been evaluated to be 2.5%. The statistical precision on the calibration constant is 0.5%. Measured with the analysis presented in this paper, the integrated luminosity for a typical data-set spanning most of the 2012 run would be different from the values reported in the past CMS public documents by approximately 0.5%.

References

[1] CMS Collaboration, "CMS Luminosity Based on Pixel Cluster Counting - Summer 2012 Update", CMS Physics Analysis Summary CMS-PAS-LUM-12-001, (2012).

[2] C. Barschel et al., "Results of the LHC DCCT Calibration Studies",.

[3] G. Anders et al., "STUDY OF THE RELATIVE LHC BUNCH POPULATIONS FOR LUMINOSITY CALIBRATION",.

[4] ATLAS Collaboration, "Improved Luminosity Determination in pp Collisions at sqrt(s)=7 TeV Using the ATLAS Detector at the LHC", *arXiv:1302.4393, to be published in Eur. Phys. J. C.*

[5] We thank our colleagues from the ALICE, ATLAS and LHCb Collaborations and from the LHC/BE-ABP and LHC/BE-OP groups for their contributions on this topic in the context of the LHC Luminosity Measurement Calibration Working Group (LLCMWG). The documentation of their studies on orbit-drift corrections, dynamic-β corrrection and non-factorization studies is in progress.

[6] H. Bartosik and G. Rumolo, "Production of the single bunch for Van der Meer scans in the LHC injector chain", (2013). CERN-ACC-NOTE-2013-0008.

[7] CMS Collaboration, "Absolute Calibration of Luminosity Measurement at CMS: Summer 2011 Update", CMS Physics Analysis Summary CMS-PAS-EWK-11-001, (2011).

[8] M. Zanetti, "Beams Scan based Absolute Normalization of the CMS Luminosity Measurement. CMS 2010 luminosity determination", (2011).

[9] A. Jeff et al., "Longitudinal density monitor for the LHC", *Phys. Rev. Spec. Top. Accel. Beams* **15** 032803.

[10] A. Boccardi, E. Bravin, M. Ferro-Luzzi, and S. Mazzoni, "LHC Luminosity calibration using the Longitudinal Density Monitor",.

[11] W. Kozanecki, T. Pieloni and J. Wenninger, "Observation of Beam-beam Deflections with LHC Orbit Data", (2013). CERN-ATS-Note-2013-XXX PERF.

[12] W. Herr, "Beam-Beam effects and Dynamic β^*",. LHC Lumi Days 2012 (2012), https://indico.cern.ch/contributionDisplay.py?confId=162948&contribId=27.

[13] CMS Collaboration, "Inclusive W/Z cross section at 8 TeV", CMS Physics Analysis Summary CMS-PAS-SMP-12-011, (2012).